



HAL
open science

Access to Heteroleptic Fluorido-Cyanido Complexes with a Large Magnetic Anisotropy by Fluoride Abstraction

Jun-Liang Liu, Kasper S Pedersen, Samuel M Greer, Itziar A Oyarzabal, Abhishake Mondal, Stephen Hill, Fabrice Wilhelm, Andrei Rogalev, Alain Tressaud, Etienne Durand, et al.

► **To cite this version:**

Jun-Liang Liu, Kasper S Pedersen, Samuel M Greer, Itziar A Oyarzabal, Abhishake Mondal, et al.. Access to Heteroleptic Fluorido-Cyanido Complexes with a Large Magnetic Anisotropy by Fluoride Abstraction. *Angewandte Chemie International Edition*, 2020, 59 (26), pp.10306-10310. 10.1002/anie.201914934 . hal-02894589

HAL Id: hal-02894589

<https://hal.science/hal-02894589>

Submitted on 9 Jul 2020

HAL is a multi-disciplinary open access archive for the deposit and dissemination of scientific research documents, whether they are published or not. The documents may come from teaching and research institutions in France or abroad, or from public or private research centers.

L'archive ouverte pluridisciplinaire **HAL**, est destinée au dépôt et à la diffusion de documents scientifiques de niveau recherche, publiés ou non, émanant des établissements d'enseignement et de recherche français ou étrangers, des laboratoires publics ou privés.

Access to Heteroleptic Fluorido-Cyanido Complexes with a Large Magnetic Anisotropy by Fluoride Abstraction

Jun-Liang Liu, Kasper S. Pedersen, Samuel M. Greer, Itziar Oyarzabal, Abhishake Mondal, Stephen Hill,* Fabrice Wilhelm, Andrei Rogalev, Alain Tressaud, Etienne Durand, Jeffrey R. Long, and Rodolphe Clérac*

Abstract: Silicon-mediated fluoride abstraction is demonstrated as a means of generating the first fluorido-cyanido transition metal complexes. This new synthetic approach is exemplified by the synthesis and characterization of the heteroleptic complexes, $\text{trans-[M}^{\text{IV}}\text{F}_4(\text{CN})_2]^{2-}$ ($M = \text{Re, Os}$), obtained from their homoleptic $[\text{M}^{\text{IV}}\text{F}_6]^{2-}$ parents. As shown by combined high-field electron paramagnetic resonance spectroscopy and magnetization measurements, the partial substitution of fluoride by cyanide ligands leads to a marked increase in the magnetic anisotropy of $\text{trans-[ReF}_4(\text{CN})_2]^{2-}$ as compared to $[\text{ReF}_6]^{2-}$, reflecting the severe departure from an ideal octahedral (O_h point group) ligand field. This methodology paves the way toward the realization of new heteroleptic transition metal complexes that may be used as highly anisotropic building-blocks for the design of high-performance molecule-based magnetic materials.

The fundamental coordination chemistry of 4d and 5d transition metal ions remains much less explored and developed than that of the lighter 3d congeners. However, recent results showing the promise of heavier transition metal ions in advanced inorganic and molecule-based materials have sparked interest in engineering their physical properties,

notably their magnetic anisotropy.^[1] Potential applications of these materials are intimately connected to the electronic structure of the metal ion, which, in turn, is determined by the nature of its coordination environment. The number of homo- and heteroleptic complexes of paramagnetic 4d and 5d ions remains low,^[1,2] reflecting the synthetic complications caused by the common robustness of the complexes of heavier transition metals. Indeed, only a few approaches exist to deliberately modify the coordination environment of such metal ions. Prominent examples of the 5d series include Re^{IV} and Os^{IV} metal ions, which, for instance, are found in both $[\text{MF}_6]^{2-}$ and $[\text{M}(\text{CN})_7]^{3-}$ species.^[3,4] These two types of complexes differ not only in coordination geometry, but also in electronic structure, due to the entirely different nature of the perturbation imposed by cyanide and fluoride to the 5d orbitals, in accord with the spectrochemical series. Combining the two ligand types in a single 5d complex would provide an intriguing possibility of substantially altering their ligand field and, thus, their magnetic anisotropy.

Following this idea, we herein present the first examples of heteroleptic fluorido-cyanido complexes of any metal ion, as synthesized by a partial abstraction of coordinated fluoride ions.^[5] This work was inspired by the recent isolation of

[*] Dr. J.-L. Liu, Prof. Dr. K. S. Pedersen, Dr. I. Oyarzabal, Dr. A. Mondal, Dr. R. Clérac
Univ. Bordeaux, CNRS, Centre de Recherche Paul Pascal, CRPP,
UMR 5031, 33600 Pessac (France)
E-mail: clerac@crpp-bordeaux.cnrs.fr
Dr. I. Oyarzabal
Chemistry Faculty, University of the Basque Country UPV/EHU
20018 Donostia-San Sebastián (Spain)
Prof. Dr. S. Hill
Department of Physics, Florida State University
and
National High Magnetic Field Laboratory, Florida State University
Tallahassee, FL 32306 (USA)
E-mail: shill@magnet.fsu.edu
Dr. A. Tressaud, E. Durand
CNRS, ICMCB, UPR 9048, Univ. Bordeaux, 33608 Pessac (France)
Prof. Dr. J. R. Long
Department of Chemistry, University of California Berkeley (USA)
and
Department of Chemical and Biomolecular Engineering,
University of California Berkeley (USA)
and
Materials Sciences Division, Lawrence Berkeley National Laboratory
Berkeley, CA 94720 (USA)
Dr. F. Wilhelm, Dr. A. Rogalev
ESRF-The European Synchrotron, 38043 Grenoble Cedex 9 (France)

Dr. J.-L. Liu
Current address: Key Laboratory of Bioinorganic and Synthetic
Chemistry of Ministry of Education, School of Chemistry,
Sun Yat-Sen University, Guangzhou 510275 (P. R. China)
Prof. Dr. K. S. Pedersen
Current address: Department of Chemistry,
Technical University of Denmark, 2800, Kgs. Lyngby (Denmark)
Dr. A. Mondal
Current address: Solid State and Structural Chemistry Unit,
Indian Institute of Science
C.V. Raman Road, Bangalore-560012 (India)
Dr. S. M. Greer
Department of Chemistry, Florida State University
and
National High Magnetic Field Laboratory, Florida State University
Tallahassee, FL 32306 (USA)

heteroleptic fluorido-cyanido anions of main-group elements, which were realized through fluoride abstraction from $[\text{PF}_6]^-$ using highly fluorophilic organo-silicon reagents.^[6] For example, *cis*- $[\text{PF}_2(\text{CN})_4]^-$ was isolated by the reaction of $[\text{PF}_6]^-$ with $(\text{CH}_3)_3\text{SiCN}$ under autogenous pressure at elevated temperatures.^[6a] The driving force for this type of reaction is the difference in bond energy between the strong Si–F bond and the significantly weaker Si–C one ($\Delta H_f^{298\text{K}}(\text{Si-F}) = 540 \text{ kJ mol}^{-1}$ vs. $\Delta H_f^{298\text{K}}(\text{Si-C}) = 435 \text{ kJ mol}^{-1}$).^[7] To our knowledge, similar chemical reactivity in transition metal chemistry has never been reported.

The reaction of $(\text{PPh}_4)_2[\text{MF}_6]$ ($M = \text{Re}, \text{Os}$) with eight equivalents of $(\text{CH}_3)_3\text{SiCN}$ in dry CH_2Cl_2 at room-temperature and ambient pressure affords a single isolatable product of $(\text{PPh}_4)_2[\text{trans-MF}_4(\text{CN})_2] \cdot \text{H}_2\text{O}$ ($M = \text{Re}$ (**1**), Os (**2**)) in high yield (Figure 1 a; see the Supporting Information for details). Single-crystal X-ray diffraction structure analysis of **1** and **2** (Figure 1 b and Supporting Information, Tables S1 and S2) reveals the presence of an elongated octahedral coordination geometry for the *trans*- $[\text{MF}_4(\text{CN})_2]^{2-}$ complexes, with M–F and M–C bond distances of 1.93–1.95 Å and 2.12–2.14 Å, respectively. Fluorine elemental analyses corroborate the presence of four fluoride ligands per metal ion, which is further supported by the isotope patterns observed in electrospray mass spectra (Supporting Information, Figures S2 and S3).^[8]

The magnetic properties of these two unique heteroleptic complexes were probed using static (dc) magnetic susceptibility measurements. For **1**, the magnetic susceptibility-temperature product, χT , remains nearly constant from room temperature down to approximately 100 K (1.18 – $1.12 \text{ cm}^3 \text{ K mol}^{-1}$, see Figure 2 a). Considering a pure $S = 3/2$ spin ground state for the Re^{IV} magnetic center, the average g -factor can be estimated from the room-temperature χT value to be 1.58. Upon further cooling from 100 K, χT drops steadily to reach $0.78 \text{ cm}^3 \text{ K mol}^{-1}$ at 1.85 K. Given the absence of any close contacts between the complexes in the unit cell, this

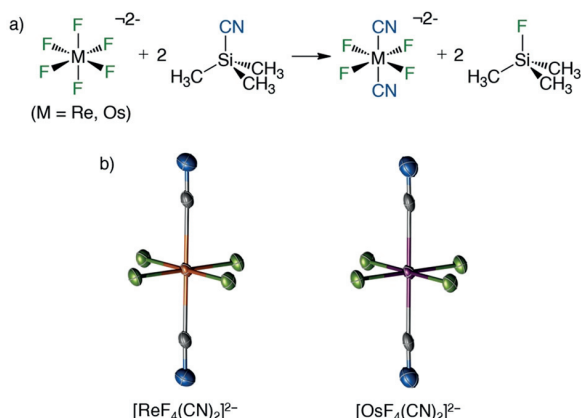


Figure 1. a) Synthesis of *trans*- $[\text{MF}_4(\text{CN})_2]^{2-}$ from the reaction of $[\text{MF}_6]^{2-}$ ($M = \text{Re}, \text{Os}$) with $(\text{CH}_3)_3\text{SiCN}$; b) View of the *trans*- $[\text{MF}_4(\text{CN})_2]^{2-}$ molecular structure in **1** and **2** from their X-ray crystal structure with thermal ellipsoids drawn at the 50% probability level (Re orange, Os purple, F green, N blue, C grey). Selected bond lengths (Å) for **1**: Re–F 1.936(1), 1.951(1); Re–C 2.135(2); C–N 1.140(3), and for **2**: Os–F 1.926(1), 1.937(1); Os–C 2.115(3); C–N 1.086(3).^[18]

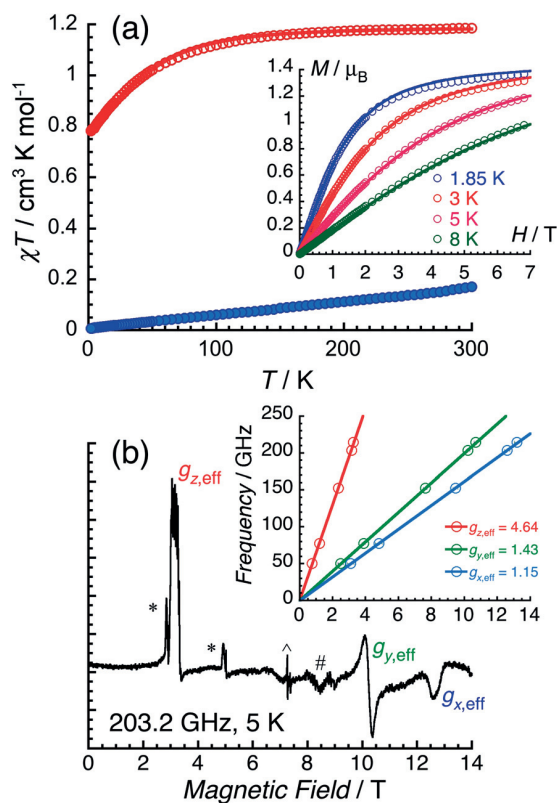


Figure 2. a) Temperature dependence of the χT product at 0.1 T for **1** (red) and **2** (blue). Inset: Field (H) dependence of the magnetization (M) below 8 K for **1**. The solid lines are the best fit of the data for **1**, as described in the main text. b) High-field electron paramagnetic resonance (HF-EPR) spectrum obtained on a powdered sample of **1** at 5 K and 203.2 GHz; the inset shows the field dependence of the resonances and the fits yielding the effective g -factors, as described in the main text. In addition to the spectral features originating from **1** (designated $g_{x,\text{eff}}$, $g_{y,\text{eff}}$, and $g_{z,\text{eff}}$), signals from molecular dioxygen (*), a common $g = 2$ impurity (^), as well as an unidentified contribution (#) are observed.

behavior indicates the presence of a large zero-field splitting of the $^4A_{2g}(O_h)$ ground state. For **2**, the magnetic measurements reveal a room temperature χT product of $0.17 \text{ cm}^3 \text{ K mol}^{-1}$, which decreases close to linearly with decreasing temperature and vanishes at the lowest temperatures ($0.0063 \text{ cm}^3 \text{ K mol}^{-1}$ at 1.85 K). This thermal behavior is expected for a $^3T_{1g}(O_h)$ term in the presence of strong spin-orbit coupling that energetically isolates a non-magnetic $J_{\text{eff}} = 0$ ground state, leaving only a temperature independent paramagnetic contribution.^[3b]

A quantitative analysis of the magnetic data for **1** was undertaken using the following spin-Hamiltonian [Eq. (1)]:

$$\hat{H} = D \left(\hat{S}_z^2 - \frac{1}{3} S(S+1) \right) + E \left(\hat{S}_x^2 - \hat{S}_y^2 \right) + \mu_B \left(g_x \hat{S}_x H_x + g_y \hat{S}_y H_y + g_z \hat{S}_z H_z \right) \quad (1)$$

This Hamiltonian contains five free variables including the zero-field splitting (ZFS) parameters D and E , and the three components of the g -tensor: g_x , g_y , and g_z . The relatively

featureless χT versus T and field-dependent magnetization plots (Figure 2a) do not provide sufficient constraints on the five parameters in Equation (1). To mitigate this problem, high-field electron paramagnetic resonance (HF-EPR) spectra of polycrystalline **1** were collected in magnetic fields up to 14 T, with multiple frequencies between 50 and 214 GHz (Figure 2b). Due to the sizable ZFS, only transitions between the components of the lower-lying Kramers doublet are observed. Hence, the $S = 3/2$ Re^{IV} center can be treated as an effective spin-1/2 ion with g_{eff} -values: $g_{z,\text{eff}} = 4.64$, $g_{y,\text{eff}} = 1.43$, and $g_{x,\text{eff}} = 1.15$ (inset of Figure 2b). In order to avoid overparameterization, the three effective g -factors obtained from the HF-EPR data (Figure 2b) were first related to the $\gamma = E/D$ ratio and the eigen-values of the actual $S = 3/2$ g -tensor (see the Supporting Information).^[9] Subsequently, the average of the Cartesian components of this g -tensor,

$g_{\text{average}} = \sqrt{(g_x^2 + g_y^2 + g_z^2)}/3$, was fixed to the powder-averaged g -factor extracted from the static magnetic susceptibility at high temperature: $g = 1.58$ at 270 K, which leads to only eight possible γ values (Supporting Information, Figure S7). However, six of them can be excluded as they result in physically unreasonable g -values ($g_i > 2$ or $g_i \leq 1$) for a system with a less than half-filled d-shell exhibiting a quenched first-order orbital angular momentum. The two remaining solutions are characterized by $D < 0$, $E/D = \pm 0.328$, and the following g -tensor components: $g_{x(y)} = 1.45$, $g_{y(x)} = 1.59$, and $g_z = 1.69$. Indeed, these two solutions are identical as they are simply related by a permutation of the x and y axes, corresponding to a change in the sign of E (Supporting Information, Table S3).

Using the above set of initial parameters, the magnetic and spectroscopic data were simultaneously fit without any further constraints, yielding the parameters: $D/k_B = -69.5$ K (-48.3 cm^{-1}), $|E|/k_B = 22.6$ K (15.7 cm^{-1}), $g_{x(y)} = 1.46$, $g_{y(x)} = 1.60$, and $g_z = 1.69$. The best-fit results are shown in Figure 2, and the calculated effective g -values ($g_{z,\text{eff}(\text{calc})} = 4.64$, $g_{y,\text{eff}(\text{calc})} = 1.43$, $g_{x,\text{eff}(\text{calc})} = 1.15$) are in perfect agreement with the HF-EPR data. The large values of the ZFS parameters, D and E , give rise to a large energy gap, $\Delta/k_B = (2\sqrt{D^2 + 3E^2})/k_B = 160$ K (111 cm^{-1}), between the two doublets of the $S = 3/2$ state. These experimentally observed ZFS parameters are reasonably well reproduced by CASSCF/NEVPT2 calculations, which, using the effective Hamiltonian approach, predict $D/k_B = -91.0$ K (-63.2 cm^{-1}) and $E/D = 0.21$ (Supporting Information, Figure S8 and Tables S4 and S5).^[10] Remarkably, the obtained energy gap is much larger than that found for the parent $[\text{ReF}_6]^{2-}$ complex ($\Delta/k_B = 69$ K)^[3a] and the structurally related $\text{trans}[\text{ReCl}_4(\text{CN})_2]^{2-}$ complex ($\Delta/k_B = 35$ K).^[11]

The electronic structure of **1** was further studied by X-ray absorption (XAS) and X-ray magnetic circular dichroism (XMCD) spectroscopy at the L_3 ($2p_{3/2} \rightarrow 5d_{3/2,5/2}$) and L_2 ($2p_{1/2} \rightarrow 5d_{3/2}$) absorption edges of rhenium at 3 K in magnetic fields up to 17 T. As expected, the XAS spectrum (Figure 3) shows intense resonant absorption (“white lines”) at both edges. Their integrals are related to the $\langle \sum_i \mathbf{l}_i \cdot \mathbf{s}_i \rangle$ expectation value, summed over all 5d electrons, through the spin-orbit

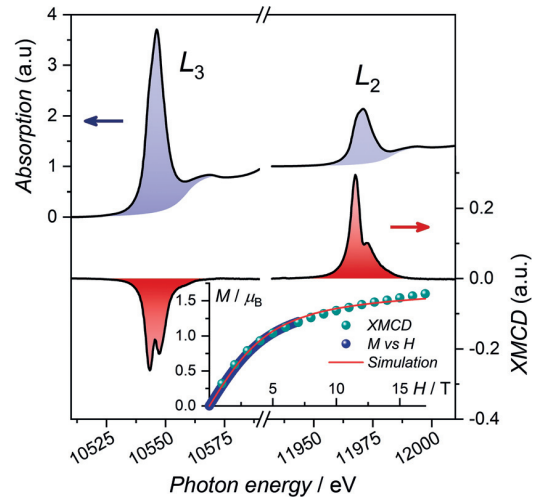


Figure 3. Isotropic XAS (top) and XMCD (bottom) spectra of a powdered sample of **1** obtained at the L_3 and L_2 rhenium absorption edges in magnetic fields of ± 17 T at 3 K. The inset shows the field dependence of the maximum dichroism signal intensity at the rhenium L_2 edge scaled to the M vs. H data obtained by magnetization measurements.

sum rule, which amounts to $\langle \sum_i \mathbf{l}_i \cdot \mathbf{s}_i \rangle / \hbar^2 = -1.56$ in **1** (see the Supporting Information),^[12] in perfect agreement with the reported value (-1.6) for the isoelectronic Os^{V} in $[\text{Os}^{\text{V}}\text{F}_6]^-$.^[3b] The XMCD spectra were recorded as the difference between two subsequent XAS spectra obtained with right and left circularly polarized X-rays and under magnetic field applied either parallel or antiparallel to the X-ray wavevector. At both the L_2 and L_3 edges, strong XMCD signals with opposite signs are observed (Figure 3). The scaling of the field-dependent XMCD signal intensity at the L_2 edge to the field dependence of the powder magnetization data at 3 K allows an estimation of the absolute value of the magnetization at 17 T (Figure 3, inset) as $1.6 \mu_B$. Through the magneto-optical sum rules,^[13] the orbital and spin magnetic moments of the rhenium 5d states could be separately determined to be $M_{\text{orbital}} = -\langle L_z \rangle \mu_B = 0.01 \mu_B$ and $M_{\text{spin}} = 1.6 \mu_B$, following the previously reported approach (see the Supporting Information).^[14] These numbers reflect the virtual total quenching of the orbital angular momentum by the ligand field which, in turn, provides the basis for neglecting orbitally dependent terms in Equation (1).

In order to probe the magnetization dynamics of **1**, alternating-current (ac) magnetic susceptibility measurements were performed. In contrast to zero-dc field, slow relaxation of the magnetization for **1** is clearly observed in the available experimental window in the presence of a static magnetic field (Figure 4 and Supporting Information, Figure S4). The field and temperature dependence of the relaxation time, τ , were estimated by fitting the $\chi'(\nu)$ and $\chi''(\nu)$ data to the generalized Debye model and their associated standard deviation was calculated from the obtained α parameter (Figure 5 and Supporting Information, Figures S5 and S6).^[15] As shown in Figure 5, the estimated standard deviation of τ is large and, thus, the following analysis of the relaxation must be taken with a certain

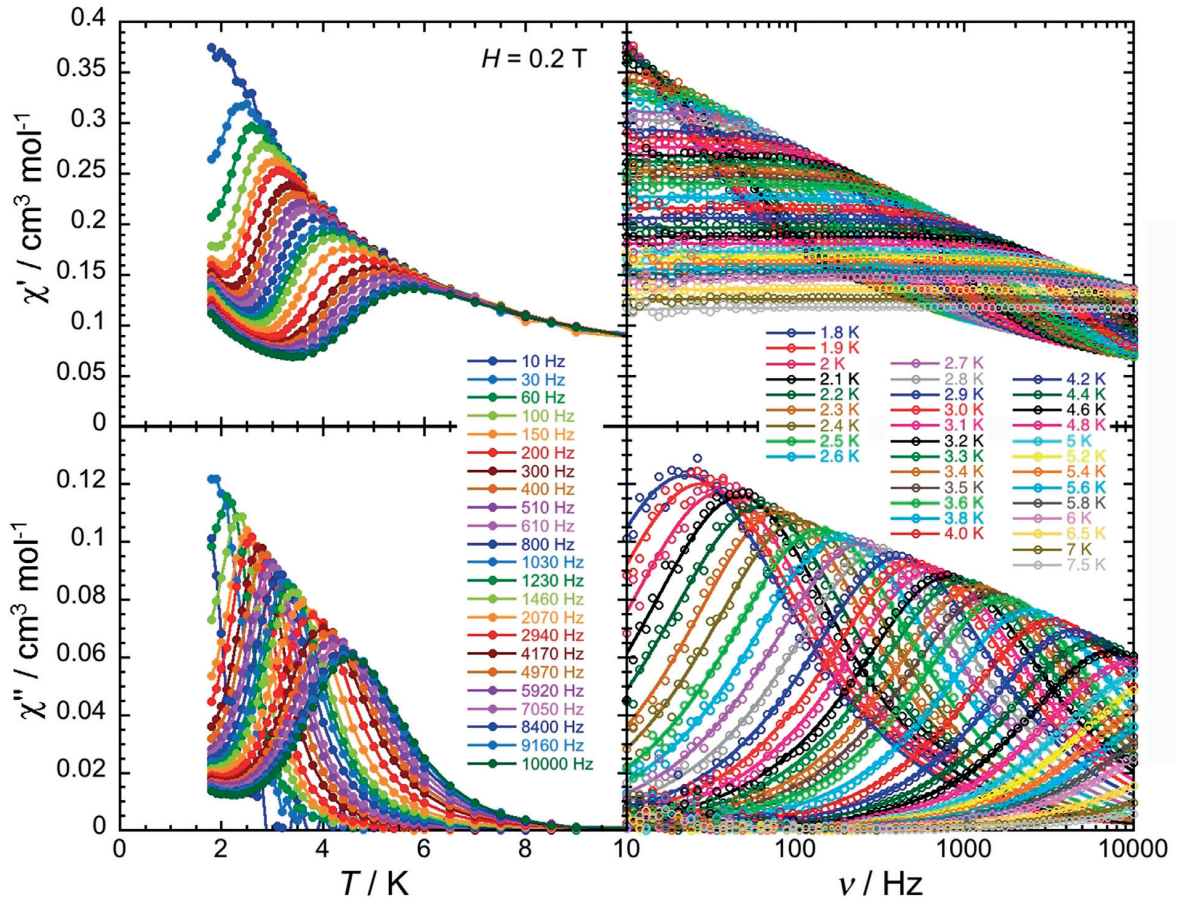


Figure 4. Temperature (left) and ac frequency (right) dependences of the real (χ' , top) and imaginary (χ'' , bottom) parts of the ac susceptibility, between 1.85 and 10 K and between 10 and 10000 Hz, for **1** in a 0.2-T dc field. Solid lines are visual guides on the left plots while they show the generalized Debye fits of the ac susceptibility data on the right.

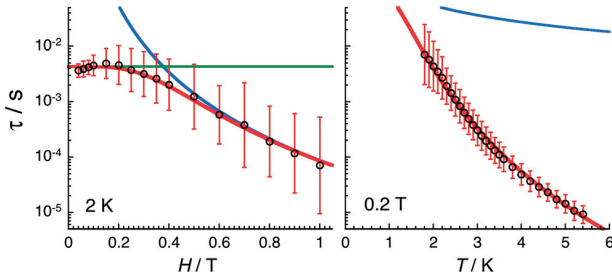


Figure 5. Field (left) and temperature (right) dependences of the relaxation time, τ , for **1** estimated from the generalized Debye fits of the ac susceptibility data shown in Figure S4 in the Supporting Information and Figure 4 collected at 2 K and under a 0.2-T applied field, respectively. The estimated standard deviation of the relaxation time (vertical red bars) were calculated from the average α parameter of the generalized Debye fit (Supporting Information, Figures S5 and S6) and a log-normal distribution as described in ref. [15]. The red line is the best fit including Raman (green line) and direct (blue line) relaxation processes, as discussed in the text.

caution. Considering the field dependence at 2 K (Figure 5, left), two regimes are clearly observed: i) below 0.2 T, the relaxation time is quasi-field-independent indicating the absence of a significant magnetization relaxation via quantum

tunneling; meanwhile, ii) above 0.2 T, τ decreases following an H^{-4} variation as expected in the case of a one-phonon direct process ($\tau_{\text{direct}}(H,T)^{-1} = AH^4T$).^[16,17] The temperature dependence of the relaxation time shown in Figure 5 and Figure S6 in the Supporting Information is more difficult to analyze as the semilogarithmic τ vs. T^{-1} plot (Supporting Information, Figure S6) does not follow a simple Arrhenius behavior compatible with an Orbach mechanism. On the other hand, the τ vs. T data at 0.2 T are almost perfectly reproduced by a power law compatible with a Raman process which, to a first approximation, can be considered as magnetic field independent ($\tau_{\text{Raman}}(H,T)^{-1} = CT^n$).^[17] Therefore, the field and temperature dependence of the relaxation time were fitted simultaneously to a model including both direct and Raman processes ($\tau(H,T)^{-1} = \tau_{\text{direct}}(H,T)^{-1} + \tau_{\text{Raman}}(H,T)^{-1} = AH^4T + CT^n$). As shown in Figure 5, the experimental τ vs. H (at 2 K) and τ vs. T (at 0.2 T) data are perfectly reproduced by this three-parameter model with $A = 5.7(3) \times 10^3 \text{ s}^{-1} \text{ K}^{-1} \text{ T}^{-4}$, $C = 2.9(3) \text{ s}^{-1} \text{ K}^{-6.3}$ and $n = 6.3(1)$. These results suggest that the paramagnetic relaxation between 1.8 and 5.4 K is governed in **1** by direct and Raman processes only. Significantly, this conclusion is different from that reported for the related *trans*-[ReCl₄(CN)₂]²⁻ complex, wherein the Orbach process ($\tau_0 = 5.7 \times 10^{-11} \text{ s}$, and $\Delta_{\text{eff}}/k_B =$

39 K) dominates over similar Raman and direct mechanisms ($A = 29 \times 10^3 \text{ s}^{-1} \text{ K}^{-1} \text{ T}^{-4}$, $C = 2.5 \text{ s}^{-1} \text{ K}^{-6.9}$ and $n = 6.9$), likely due to the much smaller energy splitting between the two Kramers doublets (39 K) than for **1** (160 K).^[11b]

In summary, the first two fluorido-cyanido transition metal complexes have been realized through silicon-mediated fluoride abstraction. The structural and magnetic properties of these heteroleptic complex salts, $(\text{PPh}_4)_2[\text{trans-M}^{\text{IV}}\text{F}_4(\text{CN})_2] \cdot \text{H}_2\text{O}$ ($M = \text{Re}$ and Os), have been studied in great detail. For the Re^{IV} compound, the combined analysis of high-field EPR and magnetization data circumvents the common problem of overparameterization of powder- and thermodynamically averaged magnetization data and provides an unambiguous determination of the zero-field splitting parameters and g -tensor. Notably, the measured magnetic anisotropy, reflected by the 160 K energy gap between the two doublets of the $S = 3/2$ ground state, is one of the largest known for a 5d transition metal complex,^[2c,3a,11] which illustrates the viability of our synthetic methodology to target new heteroleptic transition metal complexes with strong magnetic anisotropy.

Acknowledgements

K.S.P. and R.C. thank the Danish Research Council for Independent Research for a DFF-Sapere Aude Research Talent grant (4090-00201), the University of Bordeaux, the ANR, the CNRS, the Region Nouvelle Aquitaine, the MOLSPIN COST action CA15128 and the GdR MCM-2. Research at the University of California, Berkeley was supported by NSF Grant CHE-1800252 to J.R.L. A portion of this work was performed at the National High Magnetic Field Laboratory, which is supported by the NSF Cooperative Agreement (DMR-1644779) and the state of Florida. R.C. and J.R.L. are grateful to the France-Berkeley Fund and the CNRS (PICS N°06485) for funding. S.M.G. acknowledges support from the NSF Graduate Research Fellowship Program (DGE-1449440). Support from the NSF (DMR-1610226 to S.H.) is also acknowledged. I.O. and R.C. are grateful to the Basque Government for a postdoctoral grant of I.O. The X-ray spectroscopy experiments were performed at the European Synchrotron Radiation Facility (ESRF, Grenoble, France). Dr. D. Sadhukhan is acknowledged for helpful discussions about the synthesis.

- Long, *J. Am. Chem. Soc.* **2010**, *132*, 3980–3988; c) J. Martínez-Lillo, T. F. Mastropietro, E. Lhotel, C. Paulsen, J. Cano, G. De Munno, F. Faus, F. Lloret, M. Julve, S. Nellutla, J. Krzystek, *J. Am. Chem. Soc.* **2013**, *135*, 13737–13748; d) J. Martínez-Lillo, F. Faus, F. Lloret, M. Julve, *Coord. Chem. Rev.* **2015**, *289*–290, 215–217.
- [3] a) K. S. Pedersen, M. Sigrist, M. A. Sørensen, A.-L. Barra, T. Weyhermüller, S. Piligkos, C. A. Thuesen, M. G. Vinum, H. Mutka, H. Weihe, R. Clérac, J. Bendix, *Angew. Chem. Int. Ed.* **2014**, *53*, 1351–1354; *Angew. Chem.* **2014**, *126*, 1375–1378; b) K. S. Pedersen, D. N. Woodruff, S. K. Singh, A. Tressaud, E. Durand, M. Atanasov, P. Perlepe, K. Ollefs, F. Wilhelm, C. Mathonière, F. Neese, A. Rogalev, J. Bendix, R. Clérac, *Chem. Eur. J.* **2017**, *23*, 11244–11248.
- [4] a) M. V. Bennett, J. R. Long, *J. Am. Chem. Soc.* **2003**, *125*, 2394–2395; b) E. V. Peresypkina, A. Gavriluta, K. E. Vostrikova, *Crystals* **2016**, *6*, 102; c) D. E. Freedman, D. M. Jenkins, A. T. Iavarone, J. R. Long, *J. Am. Chem. Soc.* **2008**, *130*, 2884–2885; d) D. G. Samsonenko, C. Paulsen, E. Lhotel, V. S. Mironov, K. E. Vostrikova, *Inorg. Chem.* **2014**, *53*, 10217–10231.
- [5] a) N. M. Doherty, N. W. Hoffman, *Chem. Rev.* **1991**, *91*, 553–573; b) J. L. Kiplinger, T. G. Richmond, C. E. Osterberg, *Chem. Rev.* **1994**, *94*, 373–431; c) E. F. Murphy, R. Murugavel, H. W. Roesky, *Chem. Rev.* **1997**, *97*, 3425–3468.
- [6] a) J. Bresien, S. Ellinger, J. Harloff, A. Schulz, K. Sievert, A. Stoffers, C. Täschler, A. Villinger, C. Zur Täschler, *Angew. Chem. Int. Ed.* **2015**, *54*, 4474–4477; *Angew. Chem.* **2015**, *127*, 4556–4559; b) J. Harloff, D. Michalik, S. Nier, A. Schulz, P. Stoer, A. Villinger, *Angew. Chem. Int. Ed.* **2019**, *58*, 5452–5456; *Angew. Chem.* **2019**, *131*, 5506–5511.
- [7] J. A. Dean in *Lange's Handbook of Chemistry*, 15th ed., McGraw-Hill, Inc., New York; London, **1999**, pp. 4.50.
- [8] L. Patiny, A. Borel, *J. Chem. Inf. Model.* **2013**, *53*, 1223–1228.
- [9] R. Boča in *A Handbook of Magnetochemical Formulae*, Elsevier, Oxford, **2012**, pp. 189–230; J. R. Pilbrow, *J. Magn. Reson.* **1978**, *31*, 479–490.
- [10] F. Neese, *WIREs Comput. Mol. Sci.* **2018**, *8*, e1327.
- [11] a) X. Feng, J. Liu, T. D. Harris, S. Hill, J. R. Long, *J. Am. Chem. Soc.* **2012**, *134*, 7521–7529; b) X. Feng, J.-L. Liu, K. S. Pedersen, J. Nehr Korn, A. Schnegg, K. Holldack, J. Bendix, M. Sigrist, H. Mutka, D. Samohvalov, D. Aguilà, M.-L. Tong, J. R. Long, R. Clérac, *Chem. Commun.* **2016**, *52*, 12905–12908.
- [12] G. van der Laan, B. T. Thole, *Phys. Rev. Lett.* **1988**, *60*, 1977–1980.
- [13] a) B. T. Thole, P. Carra, F. Sette, G. van der Laan, *Phys. Rev. Lett.* **1992**, *68*, 1943–1946; b) P. Carra, B. T. Thole, M. Altarelli, X. Wang, *Phys. Rev. Lett.* **1993**, *70*, 694–697.
- [14] K. S. Pedersen, J. Bendix, A. Tressaud, E. Durand, H. Weihe, Z. Salman, T. J. Morsing, D. N. Woodruff, Y. Lan, W. Wernsdorfer, C. Mathonière, S. Piligkos, S. I. Klokishner, S. Ostrovsky, K. Ollefs, F. Wilhelm, A. Rogalev, R. Clérac, *Nat. Commun.* **2016**, *7*, 12195.
- [15] D. Reta, N. F. Chilton, *Phys. Chem. Chem. Phys.* **2019**, *21*, 23567–23575.
- [16] A. Abragam, B. Bleaney, *Electron Paramagnetic Resonance of Transition Ions*, Dover, New York, **1986**.
- [17] K. N. Shrivastava, *Phys. Status Solidi A* **1983**, *117*, 437–458.
- [18] CCDC 1531669 (**1**) and 1531670 (**2**) contain the supplementary crystallographic data for this paper. These data are provided free of charge by The Cambridge Crystallographic Data Centre.

[1] X.-Y. Wang, C. Avendaño, K. R. Dunbar, *Chem. Soc. Rev.* **2011**, *40*, 3213–3238.

[2] a) M. P. Shores, J. J. Sokol, J. R. Long, *J. Am. Chem. Soc.* **2002**, *124*, 2279–2292; b) T. D. Harris, M. V. Bennett, R. Clérac, J. R.

Supporting Information

Access to Heteroleptic Fluorido-Cyanido Complexes with a Large Magnetic Anisotropy by Fluoride Abstraction

Jun-Liang Liu, Kasper S. Pedersen, Samuel M. Greer, Itziar Oyarzabal, Abhishake Mondal, Stephen Hill, Fabrice Wilhelm, Andrei Rogalev, Alain Tressaud, Etienne Durand, Jeffrey R. Long, and Rodolphe Clérac**

Table of Contents

1. Synthesis and characterization	S2
2. Crystallographic Data.....	S3
3. Infrared Spectroscopy.....	S4
4. Mass Spectrometry	S5
5. EPR Measurements.....	S6
6. Additional magnetic Data	S6
7. Correlations between Real and Effective g -Tensors.....	S9
8. CASSCF/NEVPT2 Calculations.....	S11
9. X-ray spectroscopy	S13
10. References.....	S13

1. Synthesis and characterization

The compounds $(\text{PPh}_4)_2[\text{ReF}_6] \cdot 2\text{H}_2\text{O}$ and $(\text{PPh}_4)_2[\text{OsF}_6] \cdot 2\text{H}_2\text{O}$ were prepared as previously described,^[1] and dried at 100°C under vacuum on a Schlenk line to obtain desolvated precursors, $(\text{PPh}_4)_2[\text{MF}_6]$. Dichloromethane (containing less than 40 ppm of water) was purified using an Innovative Technologies solvent purification system. All other reagents and solvents were commercially available and used as received without further purification.

Synthesis of 1. The synthesis was performed under a dry argon atmosphere using standard Schlenk or glovebox techniques. $(\text{CH}_3)_3\text{SiCN}$ (0.1 mL, 0.8 mmol) was first added to a solution of $(\text{PPh}_4)_2[\text{ReF}_6]$ (196 mg, 0.20 mmol) in dichloromethane (110 mL). After stirring for 3 hours, the solvent was removed using a dynamic vacuum. A mixture of dichloromethane (60 mL) and $(\text{CH}_3)_3\text{SiCN}$ (0.1 mL, 0.8 mmol) was then added to the resulting brown solid, which dissolves. The mixture was left stirring overnight. It is worth mentioning that this two-steps reaction is working in similar manner when using less dichloromethane (12 mL in each step) leading to a $(\text{PPh}_4)_2[\text{ReF}_6]$ suspension rather than a solution. After a few hours, a light brown solution is systematically obtained.

After removal of the solvent using a dynamic vacuum, *N,N*-dimethylacetamide (2 mL; containing around 2000 ppm of water) was added to dissolve the residue, and the solution was filtered with a VWR syringe filter (25 mm, 0.2 mm PTFE). Slow addition of diethylether (50 mL; containing around 200 ppm of water) to the filtrate afforded $(\text{PPh}_4)_2[\text{trans-ReF}_4(\text{CN})_2] \cdot \text{H}_2\text{O}$ in a yield of >80%. The water molecule observed in the crystal structure most likely originates from the solvents. It is worth mentioning that a stoichiometric amount of $(\text{CH}_3)_3\text{SiCN}$ (2 equivalents) leads to a mixture of species, $[\text{MF}_{6-n}(\text{CN})_n]^{2-}$ ($n \leq 2$), while an excess of 8 up to 10 equivalents (in total for the two-step reaction) does not change the final bis-substituted product.

Crystallization of 1. Single crystals suitable for X-ray crystal structure determination were obtained by slow vapor diffusion of diethylether into a *N,N*-dimethylacetamide solution of $(\text{PPh}_4)_2[\text{trans-ReF}_4(\text{CN})_2]$ in air.. Elemental analysis: calcd (%) for $\text{C}_{50}\text{H}_{42}\text{F}_4\text{N}_2\text{OP}_2\text{Re}$: C 59.40, H 4.19, N 2.77, F 7.52; found: C 59.17, H 4.10, N 3.29, F 6.76. IR of **1** (solid, $\bar{\nu}/\text{cm}^{-1}$) 615 (m), 689 (vs), 719 (vs), 762 (vs), 856 (w), 996 (s), 1104 (vs), 1165 (w), 1190 (m), 1317 (m), 1436 (s), 1484 (m), 1585 (m), 1619 (m), 2128 (m), 3025 (w), 3064 (w), 3082 (w), 3484 (m), 3511 (m), 3557 (m).

Synthesis and crystallization of 2. The synthetic procedure and crystallization employed for **2** are identical to that of **1**, but $(\text{PPh}_4)_2[\text{ReF}_6]$ was replaced by $(\text{PPh}_4)_2[\text{OsF}_6]$. Yield: ~60%. Elemental analysis: calcd (%) for $\text{C}_{50}\text{H}_{42}\text{F}_4\text{N}_2\text{OP}_2\text{Os}$: C 59.16, H 4.17, N 2.76, F 7.49; found: C 58.73, H 4.24, N 2.72, F 7.34. IR of **2** (solid, $\bar{\nu}/\text{cm}^{-1}$) 561 (vs), 615 (m), 689 (vs), 719 (vs), 762 (s), 856 (w), 996 (s), 1105 (vs), 1165 (w), 1190 (m), 1317 (m), 1436 (s), 1484 (m), 1585 (m), 1617 (m), 2124 (m), 3025 (w), 3065 (w), 3083 (w), 3476 (m), 3510 (m), 3551 (m).

2. Crystallographic Data

Diffraction intensities were collected on a Bruker APEXII Quasar diffractometer with Mo K_{α} radiation ($\lambda = 0.71073 \text{ \AA}$) for **1** and **2** at 120 K and 122 K, respectively. The structures were solved by direct methods, and all non-hydrogen atoms were refined anisotropically by least-squares on F^2 using the SHELXTL program. Anisotropic thermal parameters were assigned to all non-hydrogen atoms. Hydrogen atoms on organic ligands were generated by the riding model.^[2] CCDC 1531669 (**1**) and 1531670 (**2**), contain the supplementary crystallographic data for this paper. These data can be obtained free of charge from The Cambridge Crystallographic Data Centre via <https://www.ccdc.cam.ac.uk/structures/>.

Table S1. Crystallographic Data and Structural Refinements for **1** and **2**.

Compound	1	2
Molecular formula	C ₅₀ H ₄₂ F ₄ N ₂ OP ₂ Re	C ₅₀ H ₄₂ F ₄ N ₂ OP ₂ Os
Formula weight	1010.99	1014.99
Crystal system	Triclinic	Triclinic
Space group	<i>P</i> -1	<i>P</i> -1
<i>a</i> / Å	9.7647(3)	9.7533(5)
<i>b</i> / Å	10.5251(3)	10.5287(5)
<i>c</i> / Å	11.5912(3)	11.5390(5)
α / °	75.5692(8)	75.641(2)
β / °	70.3354(10)	70.417(2)
γ / °	77.4645(9)	77.539(2)
<i>V</i> / Å ³	1074.76(5)	1070.04(9)
<i>Z</i>	1	1
ρ_{calcd} / g cm ⁻³	1.562	1.575
$\mu(\text{Mo } K_{\alpha})$ / mm ⁻¹	2.959	3.112
<i>F</i> 000	505	506
θ range / °	1.901-27.531	2.789-27.878
collected reflns	13734	24661
unique reflns	4910	5078
reflns [$I \geq 2\sigma(I)$]	4907	5050
params / restraints	277/0	277/0
max / min $\Delta\rho_r$ / e Å ⁻³	0.770/-0.445	0.879/-0.340
GOF	1.088	1.102
R_1 [$I \geq 2\sigma(I)$] ^(a)	0.0159	0.0212
$wR_2(\text{all data})$ ^(b)	0.0384	0.0489

^(a) $R_1 = \sum ||F_o| - |F_c|| / \sum |F_o|$, ^(b) $wR_2 = [\sum w(F_o^2 - F_c^2)^2 / \sum w(F_o^2)^2]^{1/2}$

Table S2. Selected bond lengths [Å] and bond angles [°] for **1** and **2**.

	1	2	
Re1—F1	1.9359(10)	Os1—F1	1.9258(13)
Re1—F2	1.9507(10)	Os1—F2	1.9370(13)
Re1—C1	2.1347(19)	Os1—C1	2.115(3)
F1—Re1—F2	88.79(4)	F1—Os1—F2	89.38(6)
F1—Re1—C1	90.37(6)	F1—Os1—C1	90.35(7)
F2—Re1—C1	88.94(6)	F2—Os1—C1	88.85(7)

3. Infrared Spectroscopy

The IR spectra of crystalline solids were measured on a Nicolet 6700 FT-IR at room temperature.

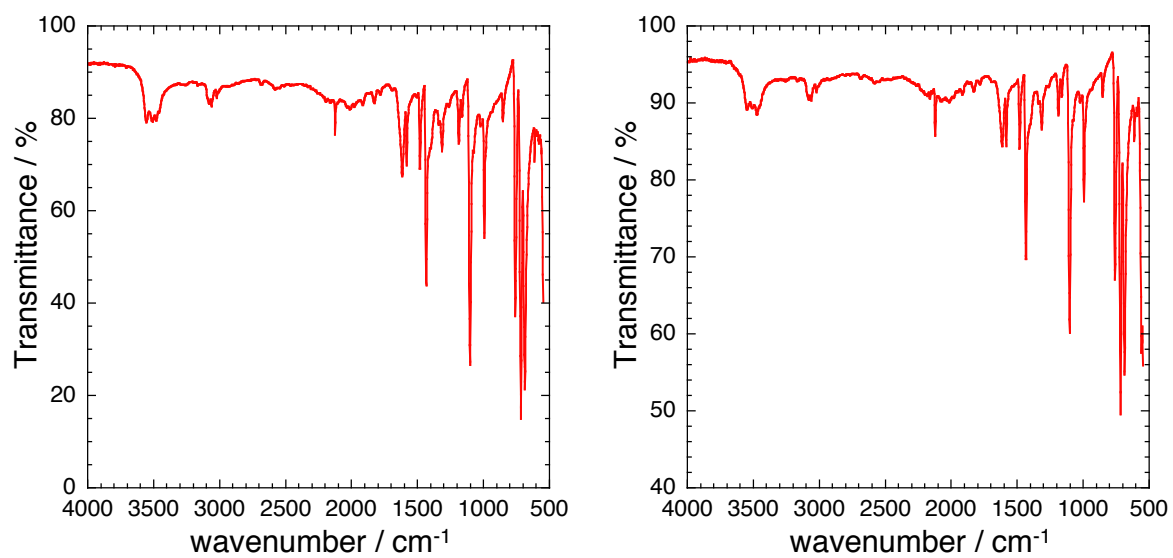


Figure S1. Room-temperature IR spectrum for **1** (*left*) and **2** (*right*) with $\bar{\nu}_{\text{CN}} = 2128$ and 2124 cm^{-1} respectively.

4. Mass Spectrometry

ESI-MS was measured on a Thermo Scientific LCQ Fleet ion trap mass spectrometer.

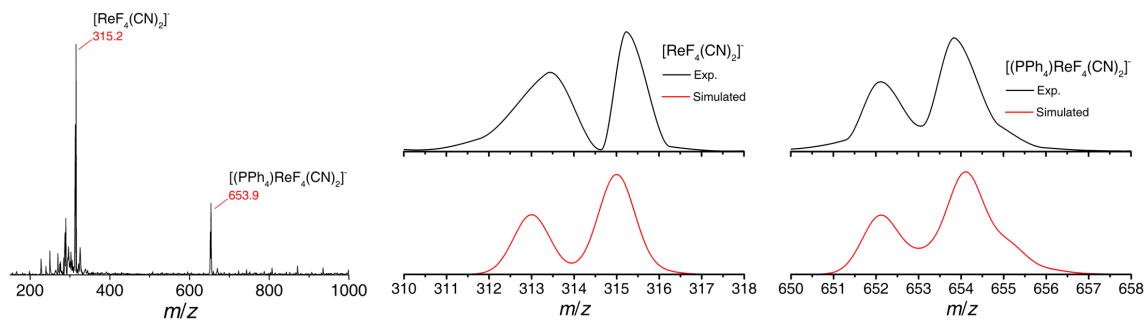


Figure S2. Mass spectrum (negative ion detection) for **1** (experimental pattern, black; simulated isotope pattern, red).

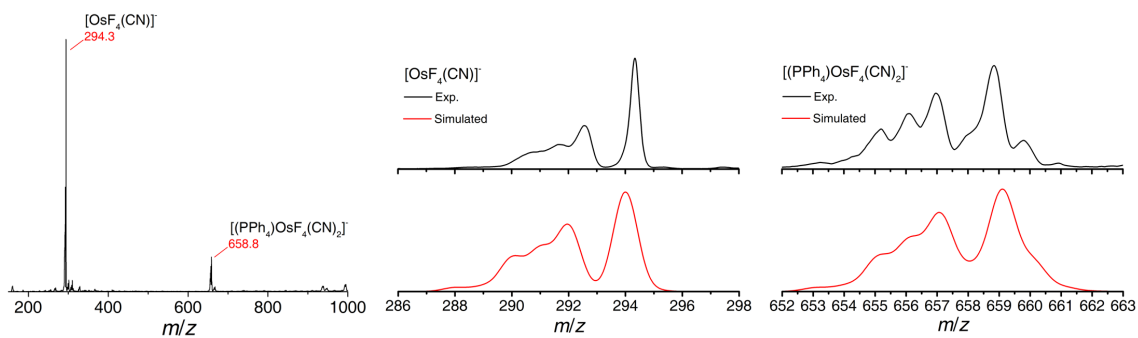


Figure S3. Mass spectrum (negative ion detection) for **2** (experimental pattern, black; simulated isotope pattern, red).

5. EPR Measurements

EPR spectra were collected on samples consisting of a microcrystalline powder suspended and frozen in mineral oil. This was done to prevent torqueing of the sample in applied fields. The transmission-type spectrometer used in this study employed a 17 T superconducting magnet in conjunction with a phase locked Virginia Diodes source combined with a series of frequency multipliers.^[3] Detection of the field modulated signal was provided by an InSb hot-electron bolometer (QMC Ltd., Cardiff, U.K.). Temperature control was accomplished using an Oxford Instruments (Oxford, U.K.) continuous-flow cryostat.

6. Additional magnetic Data

Magnetic susceptibility measurements were performed on a Quantum Design SQUID MPMS-XL magnetometer and PPMS-II susceptometer housed at the Centre de Recherche Paul Pascal at temperatures between 1.8 and 400 K and *dc* magnetic fields ranging from -9 to +9 T. The *ac* magnetic susceptibility measurements were performed in an oscillating *ac* field of 1 to 6 Oe with frequencies between 10 and 10000 Hz and various *dc* fields (including zero). The measurements were carried out on polycrystalline samples (13.44, 23.10 for **1**, and 18.94 mg for **2**) suspended in mineral oil (typically 5-15 mg) and introduced in a sealed polyethylene bag (3 × 0.5 × 0.02 cm; typically, 27-30 mg). Prior to the experiments, the field-dependent magnetization was measured at 100 K on each sample in order to detect the presence of any bulk ferromagnetic impurities. In fact, paramagnetic or diamagnetic materials should exhibit a perfectly linear dependence of the magnetization that extrapolates to zero at zero *dc* field; the samples appeared to be free of any ferromagnetic impurities. The magnetic susceptibilities were corrected for the sample holder, the mineral oil and the intrinsic diamagnetic contributions.

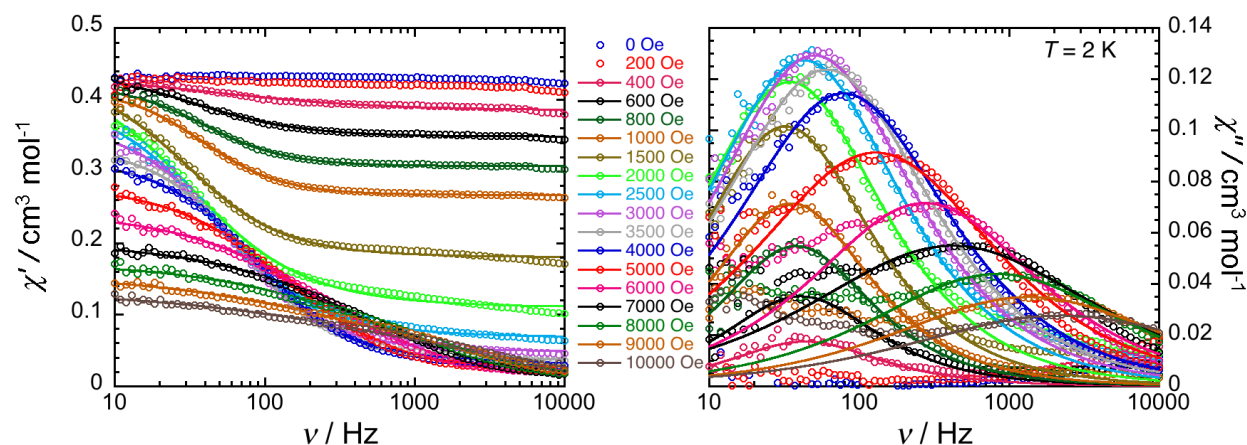


Figure S4. Frequency dependence of the real (χ' , left) and imaginary (χ'' , right) parts of the ac susceptibility for **1** collected at 2 K and varying *dc* fields. Solid lines are the best fits obtained with the generalized Debye model.

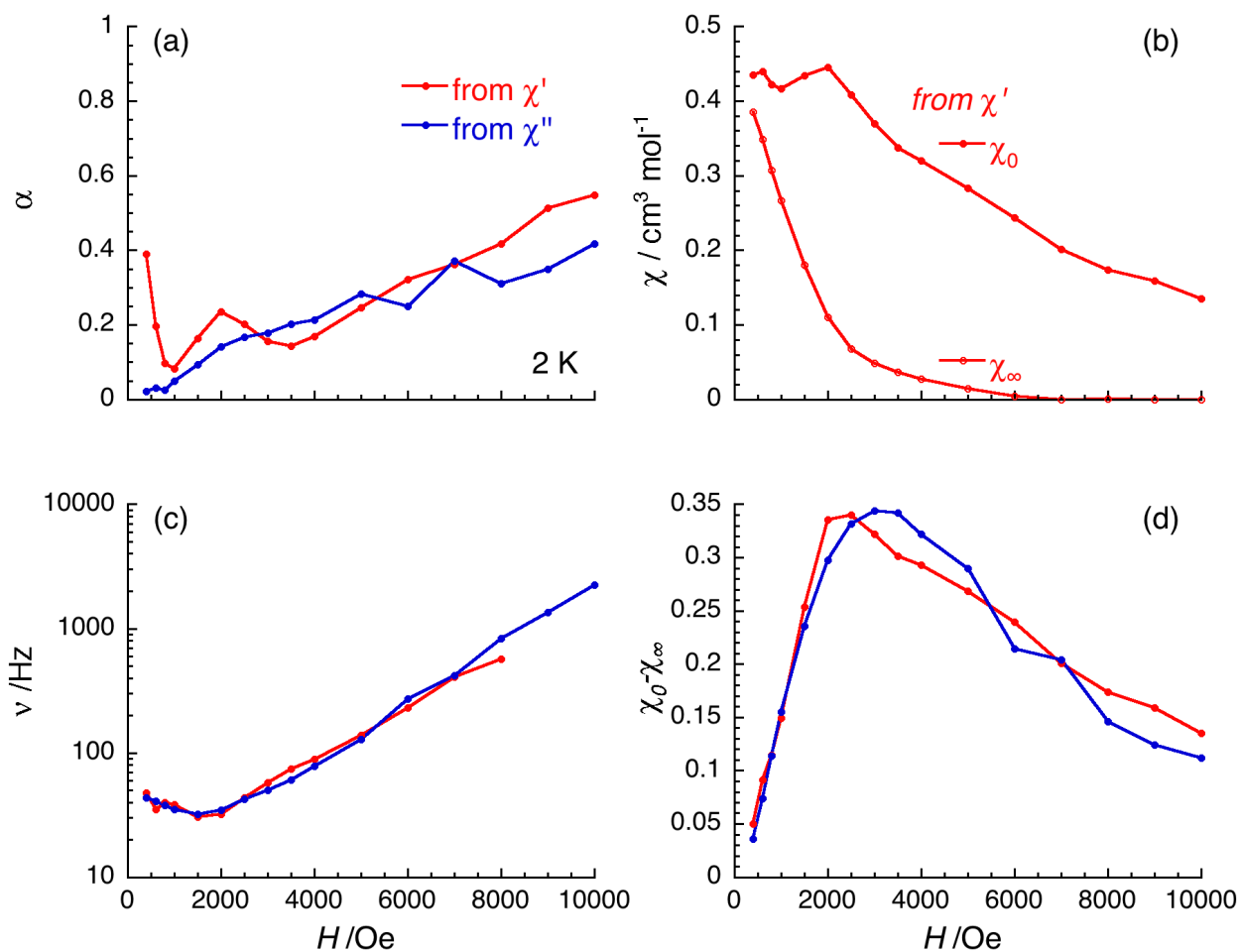


Figure S5. Field dependence of the parameters, α (a), ν (b), χ_0 & χ_∞ (c) and $\chi_0 - \chi_\infty$ (d) between 0 and 1 T deduced from the generalized Debye fit of the frequency dependence of the real (χ') and imaginary (χ'') components of the ac susceptibility at 2 K, shown in [Figure S4](#) for **1**.

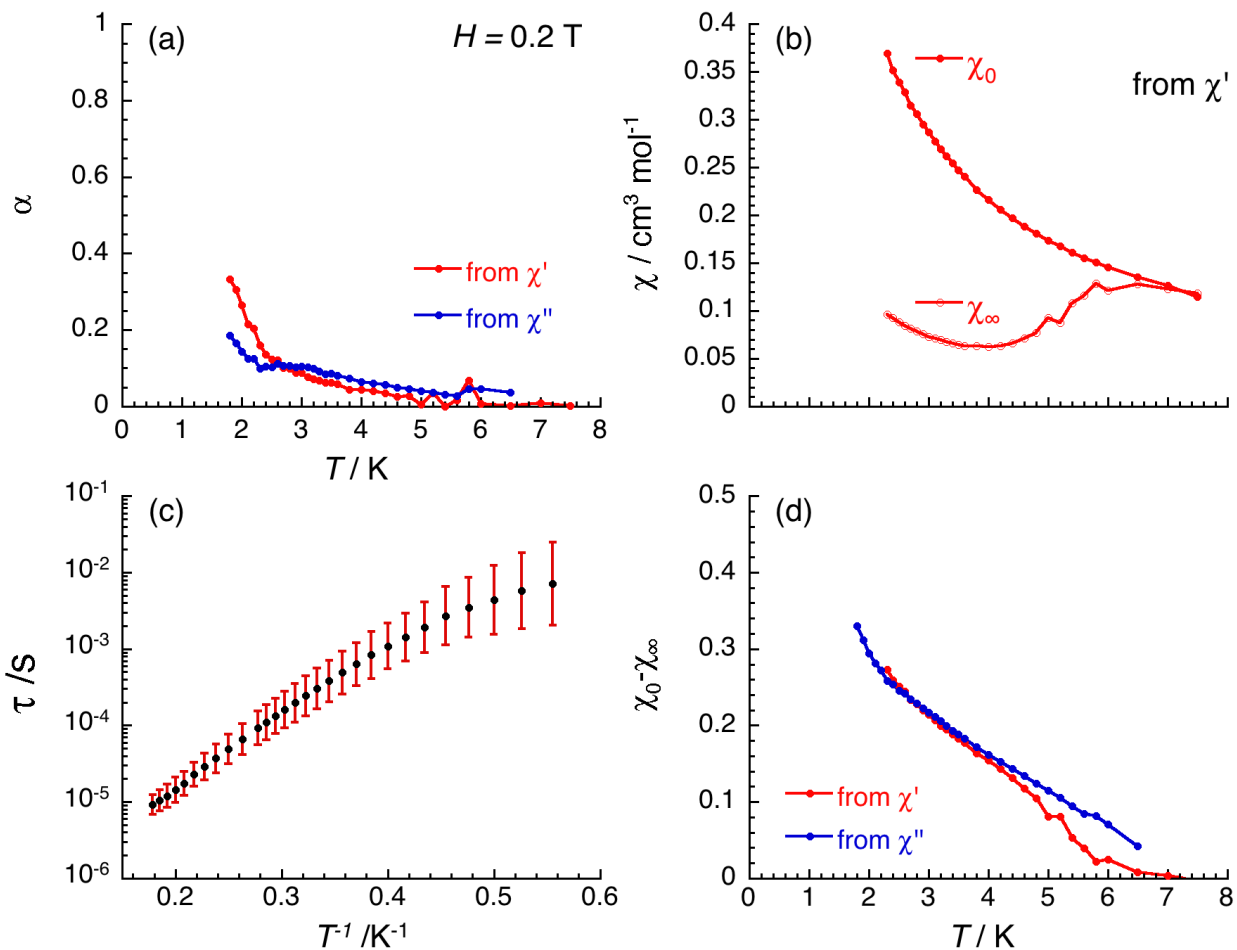


Figure S6. Temperature dependence of the parameters, α (a), χ_0 & χ_∞ (b), τ (c) and $\chi_0 - \chi_\infty$ (d) between 1.85 and 8 K deduced from the generalized Debye fit of the frequency dependence of the real (χ') and imaginary (χ'') components of the ac susceptibility at 0.2 T, shown in Figure 4 of the main text for **1**. On the bottom left figure, the temperature dependence of the relaxation time of **1** is shown at 0.2 T between 1.8 and 5.4 K (treatment of χ' versus ν and χ'' versus ν curves give undistinguishable results; both sets of data were averaged and plotted). The estimated standard deviations of the relaxation time (vertical solid bars) have been calculated from the α parameters of the generalized Debye fit (Figure 4) and the log-normal distribution as described in reference 4. The solid lines are guides for the eye.

7. Correlations between Real and Effective g -Tensors

For an $S = 3/2$ system, which is the case of the complex **1**, the spin Hamiltonian can be written as follows:

$$\hat{H} = D \left(\hat{S}_z^2 - \frac{1}{3}S(S+1) \right) + E \left(\hat{S}_x^2 - \hat{S}_y^2 \right) + \mu_B (g_x \hat{S}_x H_x + g_y \hat{S}_y H_y + g_z \hat{S}_z H_z)$$

The correlations between real and effective g -tensors are as follows:^[5]

1) $D > 0$:

$$g_{x,eff} = g_x \left| \left(1 + \frac{1-3\gamma}{\sqrt{1+3\gamma^2}} \right) \right|; g_{y,eff} = g_y \left| \left(1 + \frac{1+3\gamma}{\sqrt{1+3\gamma^2}} \right) \right|; g_{z,eff} = g_z \left| \left(1 - \frac{2}{\sqrt{1+3\gamma^2}} \right) \right|$$

2) $D < 0$:

$$g_{x,eff} = g_x \left| \left(1 - \frac{1-3\gamma}{\sqrt{1+3\gamma^2}} \right) \right|; g_{y,eff} = g_y \left| \left(1 - \frac{1+3\gamma}{\sqrt{1+3\gamma^2}} \right) \right|; g_{z,eff} = g_z \left| \left(1 + \frac{2}{\sqrt{1+3\gamma^2}} \right) \right|$$

where $\gamma = E/D$.

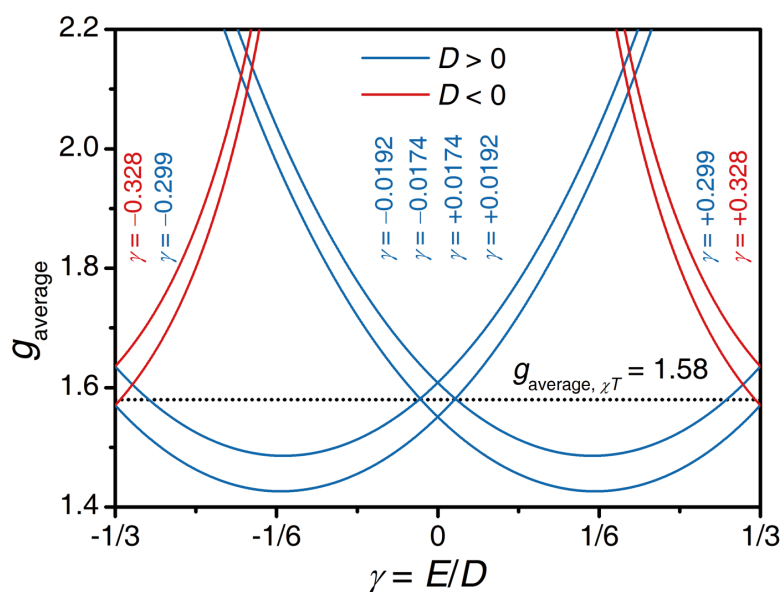


Figure S7. The plot of the calculated average g -factor (g_{average}) as function of the $\gamma = E/D$ value. According to the correlations between the real and the effective g -tensors mentioned above, the solid lines correspond to the possible scenarios in consideration of the effective g -tensors extracted from powder EPR for **1**, where $g_{\text{average}} = [(g_x^2 + g_y^2 + g_z^2)/3]^{1/2}$. The dashed line corresponds to the average g -factor (1.58) obtained from the experimental χT value (1.18 cm³ mol⁻¹ K) at 270 K. The eight intersections of solid lines and the dashed line (in the range $-1/3 < \gamma < 1/3$) are the possible solutions, which are simultaneously in perfect agreement with both EPR and magnetic susceptibility (Table S3).

Table S3. Some possible $\gamma = E/D$ value and g -tensors from Figure S7.

No.	$\gamma = E/D$	D sign	E sign	g_x	g_y	g_z	g_{average}	Note
1	-0.328	-	+	1.59	1.45	1.69	1.58	Most probable set of parameters.
2	-0.299	+	-	1.73	1.05	1.84	1.58	1) g_y is unphysically small 2) the g -tensor is too anisotropic
3	-0.0192	+	-	2.26	0.59	1.43	1.58	1) g_x is unphysically large 2) g_y is unphysically small 3) the g -tensor is too anisotropic
4	-0.0174	+	-	0.70	2.38	1.15	1.58	1) g_x is unphysically small 2) g_y is unphysically large 3) the g -tensor is too anisotropic
5	+0.0174	+	+	2.38	0.70	1.15	1.58	Physically identical to set No.4: Permutation of the x and y axes and change of E sign.
6	+0.0192	+	+	0.59	2.26	1.43	1.58	Physically identical to set No.3: Permutation of the x and y axes and change of E sign.
7	+0.299	+	+	1.05	1.73	1.84	1.58	Physically identical to set No.2: Permutation of the x and y axes and change of E sign.
8	+0.328	-	-	1.45	1.59	1.69	1.58	Physically identical to set No.1: Permutation of the x and y axes and change of E sign.

8. CASSCF/NEVPT2 Calculations

All calculations were performed using the ORCA v4.0 program package.^[6] The unoptimized crystal structure was used as the input geometry. The SA-CASSCF calculations were performed using the all-electron def2-TZVP basis set for carbon, nitrogen, and fluorine, while the SARC-TZVP basis set was used for rhenium.^[7,8] Scalar relativistic effects were accounted for with the second-order Douglas-Kroll-Hess (DKH) procedure. To speed up the calculation the resolution of identity approximation was employed.^[9] The auxiliary basis sets were generated using the 'autoaux' command as implemented in ORCA4.0.^[10] The active space was defined to include the three 5d-electrons and the five 5d-orbitals (CAS(3,5)). All 10 quartet and all 40 doublet states were calculated. To account for dynamic correlations N-electron valence perturbation theory to the second order (NEVPT2) was performed on the converged CASSCF wavefunction. Spin-orbit coupling was treated using the mean field approximation as implemented in ORCA.^[11] The results of these calculations are summarized in Figure S8 and Tables S4 and S5.

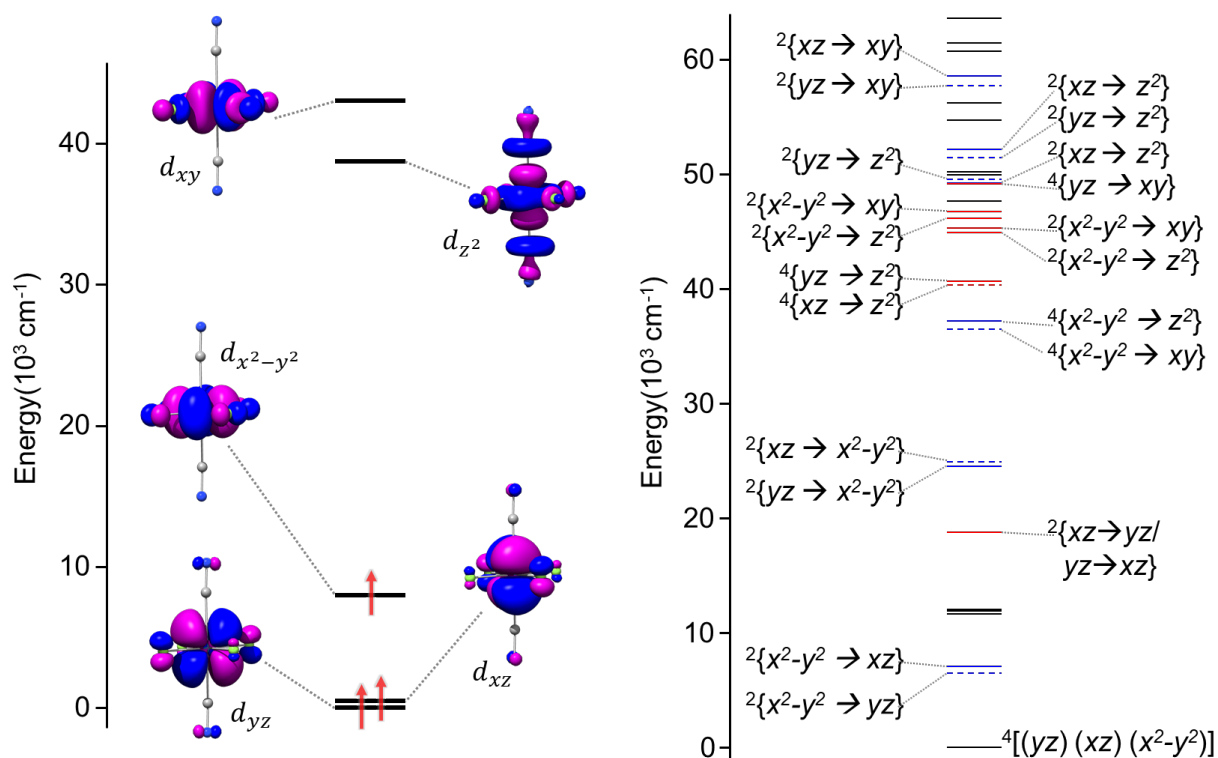


Figure S8. (Left) Qualitative MO diagram resulting from a SA-CASSCF/NEVPT2 calculation depicting the dominant configuration of the ground state. (Right) Energies of the 10 quartet 40 doublet states where the labels correspond to the excitation that best describes the main configuration of the excited state. Only states which contribute $> 1 \text{ cm}^{-1}$ to D are labelled. The ground state is labelled with the dominant configuration. The lines representing the energies of the excited states are coloured according to their contribution to D : red (positive), blue (negative) and negligible/zero (black). Furthermore, red/blue coloured states with dashed lines make negative contributions to E , while those depicted with solid lines make positive contributions. The numerical values for these contributions are shown in Table S4.

Table S4. Contributions^{^*} to D and E for the excitations indicated in [Figure S8](#).

Mult.	Transition	Energy (cm ⁻¹)	D (cm ⁻¹)	E (cm ⁻¹)
4	[(yz) (xz) (x ² -y ²)]	0	0	0
2	{x ² -y ² → yz}	6497	-82.66	-76.96
2	{x ² -y ² → xz}	7058	-67.58	62.07
2	{xz→yz}/{yz→xz}	18744	216.49	0.69
2	{yz → x ² -y ² }	24534	-67.58	9.20
2	{xz → x ² -y ² }	24939	-64.30	-15.04
4	{x ² -y ² → xy}	36495	-153.92	-0.34
4	{x ² -y ² → z ² }	37157	-2.41	0.07
4	{xz → z ² }	40313	58.16	-46.96
4	{yz → z ² }	40615	55.61	44.90
2	{x ² -y ² → z ² }	44906	8.98	0.02
2	{x ² -y ² → xy}	45259	5.39	0.01
2	{x ² -y ² → z ² }	46139	2.31	0.01
2	{x ² -y ² → xy}	46757	82.18	0.17
4	{yz → xy}	49189	2.47	0.42
2	{xz → z ² }	49202	-30.84	30.16
2	{yz → z ² }	49557	-29.54	-27.62
2	{yz → z ² }	51406	-4.06	-3.42
2	{xz → z ² }	52122	-7.63	4.05
2	{yz → xy}	57667	-2.26	-0.72
2	{xz → xy}	58503	-1.12	0.54
Total			-80.21	-20.05 (^{E/D} = 0.25)

[^]Only states with contributions larger than 1 cm⁻¹ are shown. * These contributions are calculated by second order perturbation theory. They do not add up to the total due to the neglect of numerous states with small contributions. While we have chosen this method for examining the individual contributions to D , we note that the effective Hamiltonian approach is the method used for the quoted value of D in the main text.

Table S5. Calculated zero-field splitting parameters.

	2PT [*]		Effective [^]	
	D (cm ⁻¹)	E/D	D (cm ⁻¹)	E/D
CASSCF	-56.7	0.24	27.4	0.30
NEVPT2	-80.2	0.25	-63.2	0.21

* D is calculated using second order perturbation theory (2PT).

[^] D is calculated using an effective Hamiltonian.

9. X-ray spectroscopy

The rhenium $L_{2,3}$ X-ray absorption (XAS) and X-ray magnetic circular dichroism (XMCD) spectra of **1** were recorded at the ID12 beamline at ESRF – The European Synchrotron, Grenoble, France, using total fluorescence yield detection and in magnetic fields up to ± 17 T. As the source of circularly polarized X-rays, we used the second harmonic of the emission from a helical undulator of APPLE-II type. The XMCD spectra were obtained as the direct difference between two consecutive XAS spectra recorded with right and left circularly polarized photons, using both magnetic field directions to ensure the absence of experimental artefacts. The isotropic XAS spectra were normalized to zero before the absorption edge and to unity far above the edge. The energy positions of the step functions relating the transitions into the continuum were defined as previously described.^[1b] The integral of the white line at the L_2 edge was divided by two due to the occupation ratios of $2p_{3/2}$ and $2p_{1/2}$ core states. Since the magneto-optical sum rules are derived for line intensities $I(\hbar\omega)$ ($\hbar\omega$ is the photon energy) and not for the absorption cross sections, $\mu(\hbar\omega)$, an additional correction was utilized according to $I(\hbar\omega) = 1/(4\pi^2\alpha\hbar\omega) \times \mu(\hbar\omega)$. The integral of the isotropic XAS spectra are related to the $\langle \sum_i \mathbf{l}_i \cdot \mathbf{s}_i \rangle$ expectation value, summed over all 5d electrons, through the spin-orbit sum rule, which amounts to -1.56 in **1**.^[12] It is worth mentioning that this value is very close to the one (-1.6) determined for the isoelectronic $[\text{Os}^{\text{V}}\text{F}_6]^{2-}$.^[1b] The $\langle \sum_i \mathbf{l}_i \cdot \mathbf{s}_i \rangle$ expectation value depends on the electron distribution over the spin-orbit split 5d states, $5d_{3/2}$ and $5d_{5/2}$, and can be expressed in the electron occupation numbers $\langle \sum_i \mathbf{l}_i \cdot \mathbf{s}_i \rangle / \hbar^2 = -3/2n_e^{3/2} + n_e^{5/2}$, where $n_e^{3/2} + n_e^{5/2} = n_e$ is the number of electrons in the 5d level. Given the strongly ionic nature of the complex, n_e was approximated to 3 leading to 1.82 and 1.18 for $n_e^{3/2}$ and $n_e^{5/2}$, respectively. An identical procedure was used for the normalization of the corresponding XMCD integrals to deduce spin and orbital moments:^[12]

$$\langle L_z \rangle = -\frac{2n_h}{3} \times \frac{I_{L_3}^{\text{XMCD}} + I_{L_2}^{\text{XMCD}}}{I_{L_3}^{\text{XAS}} + I_{L_2}^{\text{XAS}}}$$
$$\langle S_{\text{eff}} \rangle = -n_h \times \frac{I_{L_3}^{\text{XMCD}} - 2 \times I_{L_2}^{\text{XMCD}}}{I_{L_3}^{\text{XAS}} + I_{L_2}^{\text{XAS}}}$$

where $\langle S_{\text{eff}} \rangle = \langle S_z \rangle + 7/2 \langle T_z \rangle$ and $n_h = 10 - n_e$ is the number of holes in the 5d level. From these expressions the effective spin and orbital moments are calculated as $M_{\text{spin,eff}} = -2\langle S_{\text{eff}} \rangle$ and $M_{\text{orbital}} = -\langle L_z \rangle$ to yield $M_{\text{spin,eff}} = 1.1 \mu_B$ and $M_{\text{orbital}} = 0.01 \mu_B$. As the total moment was estimated at $1.6 \mu_B$ (Figure 3, inset), the M_{spin} can be evaluated as $M_{\text{total}} - M_{\text{orbital}} = 1.6 \mu_B$. This result allows an estimation of the dipole magnetic moment, $\langle T_z \rangle = (M_{\text{spin}} - M_{\text{spin,eff}})/7 = 0.07 \mu_B$. Notably, this value is significantly larger than the vanishing value found for the isoelectronic $[\text{Os}^{\text{V}}\text{F}_6]^{2-}$ complex, which may be related to the symmetry lowering in *trans*- $[\text{Re}(\text{CN})_2\text{F}_4]^{2-}$ as compared to the nearly perfectly octahedral OsF_6^- .^[1b]

10. References

- ¹ (a) K. S. Pedersen, M. Sigrist, M. A. Sørensen, A.-L. Barra, T. Weyhermüller, S. Piligkos, C. Aa. Thuesen, M. G. Vinum, H. Mutka, H. Weihe, R. Clérac, J. Bendix, *Angew. Chem. Int. Ed.* **2014**, *53*, 1351; (b) K. S. Pedersen, D. N. Woodruff, S. K. Singh, A. Tressaud, E. Durand, M. Atanasov, P. Perlepe, K. Ollefs, F. Wilhelm, C. Mathonière, F. Neese, A. Rogalev, J. Bendix, R. Clérac, *Chem. Eur. J.* **2017**, *23*, 11244.
- ² (a) G. M. Sheldrick, *Acta Crystallogr. A*, **2008**, *64*, 112; (b) G. M. Sheldrick, *SHELXTL 6.10*, Bruker Analytical Instrumentation, Madison, Wisconsin, USA, **2000**.
- ³ A. Hassan, L. Pardi, J. Krzystek, A. Sienkiewicz, P. Goy, M. Rohrer, L.-C. Brunel, *J. Magn. Reson.* **2000**, *142*, 300.
- ⁴ D. Reta, N. F. Chilton, *Phys. Chem. Chem. Phys.* **2019**, *21*, 23567-23575.

-
- ⁵ (a) T. Yamane, K. Sugisaki, H. Matsuoka, K. Sato, K. Toyota, D. Shiomi, T. Takui, *Dalton Trans.* **2018**, 47, 16429; (b) T. Yamane, K. Sugisaki, T. Nakagawa, H. Matsuoka, T. Nishio, S. Kiniyo, N. Mori, S. Yokoyama, C. Kawashima, N. Yokokura, K. Sato, Y. Kanzaki, D. Shiomi, K. Toyota, D. H. Dolphin, W.-C. Lin, C. A. McDowell, M. Tadokoro, T. Takui, *Phys. Chem. Chem. Phys.* **2017**, 19, 24769.
- ⁶ F. Neese, *Wiley Interdiscip. Rev. Comput. Mol. Sci.* **2018**, 8, e1327.
- ⁷ F. Weigend, R. Ahlrichs, *Phys. Chem. Chem. Phys.* **2005**, 7, 3297.
- ⁸ D. A. Pantazis, X. Y. Chen, C. R. Landis, F. Neese, *J. Chem. Theory Comput.* **2008**, 4, 908.
- ⁹ F. Neese, *J. Comput. Chem.* **2003**, 24, 1740.
- ¹⁰ G. L. Stoychev, A. A. Auer, F. Neese, *J. Chem. Theory Comput.* **2017**, 13, 554.
- ¹¹ B. A. Heß, C. M. Marian, U. Wahlgren, O. Gropen, *Chem. Phys. Lett.* **1996**, 251, 365.
- ¹² B. T. Thole, P. Carra, G. van der Laan, *Phys. Rev. Lett.* **1992**, 68, 1943.